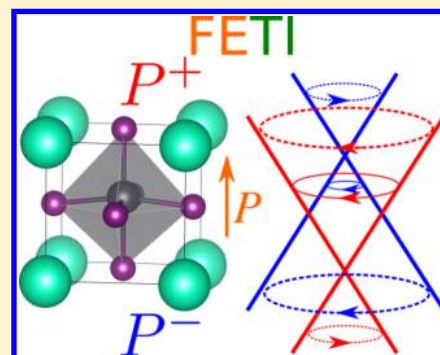


# Strain-Induced Ferroelectric Topological Insulator

Shi Liu,<sup>\*,†</sup> Youngkuk Kim,<sup>‡</sup> Liang Z. Tan,<sup>‡</sup> and Andrew M. Rappe<sup>\*,‡</sup><sup>†</sup>Geophysical Laboratory, Carnegie Institution for Science, Washington, DC 20015, United States<sup>‡</sup>The Makineni Theoretical Laboratories, Department of Chemistry, University of Pennsylvania, Philadelphia, Pennsylvania 19104–6323, United States**S** Supporting Information

**ABSTRACT:** Ferroelectricity and band topology are two extensively studied yet distinct properties of insulators. Nonetheless, their coexistence has never been observed in a single material. Using first-principles calculations, we demonstrate that a noncentrosymmetric perovskite structure of CsPbI<sub>3</sub> allows for the simultaneous presence of ferroelectric and topological orders with appropriate strain engineering. Metallic topological surface states create an intrinsic short-circuit condition, helping stabilize bulk polarization. Exploring diverse structural phases of CsPbI<sub>3</sub> under pressure, we identify that the key structural feature for achieving a ferroelectric topological insulator is to suppress PbI<sub>6</sub> cage rotation in the perovskite structure, which could be obtained via strain engineering. Ferroelectric control over the density of topological surface states provides a new paradigm for device engineering, such as perfect-focusing Veselago lens and spin-selective electron collimator. Our results suggest that CsPbI<sub>3</sub> is a simple model system for ferroelectric topological insulators, enabling future studies exploring the interplay between conventional symmetry-breaking and topological orders and their novel applications in electronics and spintronics.



**KEYWORDS:** Halide perovskites, spintronics, topological surface states, electron focusing, strain engineering

The simultaneous presence of seemingly incompatible properties of solids often provides a unique opportunity to address questions of fundamental and practical importance. The coexistence of ferroelectric and topological orders is one such example. A topological insulator (TI) is a topological state of matter that is characterized by metallic boundary modes (edge or surface) arising from the nontrivial topology of an insulating bulk electronic structure.<sup>1</sup> The metallic nature of the boundary states is protected by time-reversal symmetry, providing transport channels that are robust against ordinary nonmagnetic impurities. Fundamental scientific interest and potential applications of TIs in electronics, spintronics, and quantum information have driven tremendous efforts to find robust material realizations of TIs. To date, more than 50 candidate materials<sup>2</sup> have been suggested theoretically in diverse material classes with some confirmed experimentally, including chalcogenides,<sup>3–7</sup> oxides,<sup>8–11</sup> ternary Heusler compounds,<sup>12</sup> halide perovskites,<sup>13,14</sup> and a noncentrosymmetric Rashba semiconductor.<sup>15</sup> A characteristic feature common to these materials is a narrow band gap originating from the band inversion mechanism. Without the spin–orbit interaction, these materials would be normal insulators (NIs); the spin–orbit interaction interchanges the characters of the valence and conduction bands, resulting in a nontrivial topology. For this to occur, the band gap must be smaller than the strength of the spin–orbit interaction, typically less than 1 eV, in order to host TIs. On the other hand, ferroelectrics, which have a spontaneous macroscopic polarization switchable by an applied electric field, usually are semiconductors with a well-developed

wide band gap<sup>16–18</sup> with a few exceptions,<sup>19–21</sup> due to the large difference in electronegativity between oxygen and transition metals. Most technologically important ferroelectric materials (e.g., PbTiO<sub>3</sub> and BaTiO<sub>3</sub>) have band gaps larger than 3 eV.<sup>17</sup> The lowest band gap for a ferroelectric oxide is 1.39 eV, obtained recently in the single-phase solid oxide solution [KNbO<sub>3</sub>]<sub>1–x</sub>[BaNi<sub>1/2</sub>Nb<sub>1/2</sub>O<sub>3–δ</sub>]<sub>x</sub> (KBNNO).<sup>19</sup>

While the observed narrow band gap in various TIs seems to exclude the coexistence of ferroelectricity, there is no fundamental physics preventing the realization of both ferroelectric and topological order in a single-phase material. A ferroelectric topological insulator (FETI) that combines switchable polarization and robust topological surface states (TSSs) is likely to support novel device functionalities. Here, we demonstrate through first-principles calculations that the FETI can be realized in cubic halide perovskite CsPbI<sub>3</sub> under strain in the absence of PbI<sub>6</sub> octahedron rotation. The consequences of the coexistence of ferroelectricity and the nontrivial topology are explored. We find that the TSSs in FETI are tunable by the electrostatic potential associated with the polarity of the surfaces, which allows for simplified nanoscale engineering of topological p–n junctions<sup>22</sup> when combined with domain engineering.<sup>23</sup> Recent experiments<sup>24,25</sup> demonstrate the capability to stabilize perovskite CsPbI<sub>3</sub> under room

Received: November 7, 2015

Revised: January 14, 2016

Published: January 27, 2016



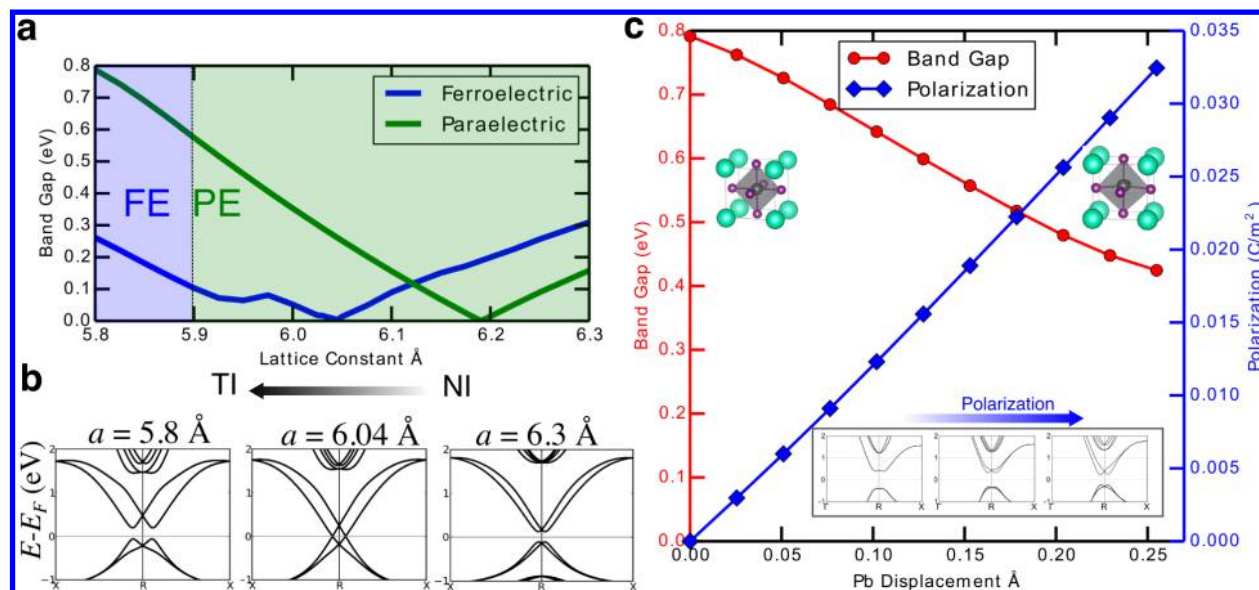


**Figure 1.** Pressure induced paraelectric–ferroelectric and trivial–nontrivial phase transitions in CsPbI<sub>3</sub>. (a) Electronic band gaps of paraelectric and ferroelectric CsPbI<sub>3</sub> as a function of lattice constant. Paraelectric CsPbI<sub>3</sub> has band gap closure at  $a = 6.19$  Å. Ferroelectric CsPbI<sub>3</sub> changes from an NI to a TI at  $a = 6.04$  Å. The system undergoes a paraelectric to ferroelectric structural phase transition as the lattice constant becomes smaller than  $\sim 5.90$  Å at room temperature. (b) Evolution of band structure of ferroelectric CsPbI<sub>3</sub> as a function of lattice constant. At  $a = 6.04$  Å, a line node (not shown) appears near the time-reversal invariant point ( $R$ ) in the Brillouin zone. (c) Electronic band gap and polarization for interpolated structures connecting paraelectric and ferroelectric CsPbI<sub>3</sub> with lattice constants fixed at 5.79 Å. Along the path, structures have gradually increasing polarization and decreasing band gaps. The inset shows the adiabatic evolution of the band structure from paraelectric to ferroelectric phase. The manifold of valence bands can be continuously transformed from paraelectric to ferroelectric without closing the band gap.

temperature, which highlights the possible realization of CsPbI<sub>3</sub>-based FETI.

Using density functional theory (DFT) calculations (see Methods), we find that the cubic halide perovskite CsPbI<sub>3</sub> experiences a paraelectric–ferroelectric structural phase transition under strain. In the absence of PbI<sub>6</sub> octahedron rotation, the cubic CsPbI<sub>3</sub> with ferroelectric distortions (Pb atom displacing away from the center of PbI<sub>6</sub> octahedron) has lower formation energy ( $\sim 10$  meV per unit cell) than the paraelectric CsPbI<sub>3</sub> for a wide range of lattice constants ( $a < 6.05$  Å) at 0 K. Free energy calculations including zero-point energy and the entropy contribution from phonons at room temperature also indicate that the system should undergo a ferroelectric distortion when the lattice constant  $a$  is compressed smaller than  $\sim 5.90$  Å.

Pressure also induces a topological phase transition from a normal insulator to a topological insulator in CsPbI<sub>3</sub>. Yang et al. and Jin et al. predicted and have shown that paraelectric CsPbI<sub>3</sub> is a topological insulator under hydrostatic pressure.<sup>13,14</sup> We find that the electronic structure of ferroelectric CsPbI<sub>3</sub> at  $a < 6.04$  Å is adiabatically connected to the topological phase of the paraelectric CsPbI<sub>3</sub>. More specifically, as shown in Figure 1c, the band gap remains open during a structural deformation from the paraelectric topological phase to the ferroelectric phase at  $a = 5.79$  Å. The bulk band structures of ferroelectric CsPbI<sub>3</sub>, calculated with varying  $a$ , also show evidence of the topological phase transition via gap closure. The bulk gap closes at  $a = 6.04$  Å (Figure 1b), exhibiting a nodal point along the  $R$ – $X$  line, and reopens for  $a < 6.04$  Å. Interestingly, a nodal point occurs not only along the high-symmetric direction but also along an arbitrary direction away from  $R$  on the  $k_z = \pi/a$  plane, forming a line node encircling  $R$ . As previously discussed,<sup>26</sup> it is a characteristic feature of topological phase transitions between NI and TI in three-dimensional noncentrosymmetric systems

that the gapless states, in general, appear off the time-reversal invariant point ( $R$ ) in a one-dimensional parameter subspace of the  $(\mathbf{k}, m)$  space, where  $m$  is an external parameter tuning a topological phase transition. Whereas the specific geometry of nodal points can depend on the details of crystalline symmetries, their formation again supports a ferroelectric topological phase at  $a < 6.04$  Å. We directly calculate the  $Z_2$  topological invariants,<sup>3</sup> employing the method proposed in ref 27. The indices are  $(\mu_0; \mu_1 \mu_2 \mu_3) = (1; 111)$ , further confirming that ferroelectric CsPbI<sub>3</sub> is a strong topological insulator under high pressure. As band gaps are systematically underestimated within DFT, electronic correlations introduced by higher level theories such as the GW approximation are expected to increase the band gap and hence lower the critical value of  $a$  at which CsPbI<sub>3</sub> becomes a TI.<sup>14</sup> Because strain favors the ferroelectric phase (in the absence of PbI<sub>6</sub> cage rotation), CsPbI<sub>3</sub> is likely to be a FETI even in the presence of electron–electron correlations.

To illustrate the TSSs of a FETI, we have calculated the surface band structures using a slab model (see Methods). Ferroelectric materials possess three different types of surfaces depending on the orientation of the polarization: nonpolar  $P^0$ , positive-polar  $P^+$ , and negative-polar  $P^-$  surfaces. We first investigate nonpolar surface states by exposing the (001) surfaces with in-plane  $[100]$  polarization (Figure 2, Top). As shown in Figure 2, the surface states exhibit a Dirac-cone-like energy dispersion at the  $\bar{M}$  point (0.5,0.5) of the surface Brillouin zone, confirming the nature of TSSs.

The surface states of the polar surfaces are studied using a (100) slab with  $[100]$ -oriented polarization (Figure 3a). Figure 3b shows the surface band structure with states from  $P^+$  (red) and  $P^-$  (blue) surfaces resolved separately for bands close to the Fermi energy (see Methods). The out-of-plane polarization breaks the degeneracy of the surface states, shifting upward in

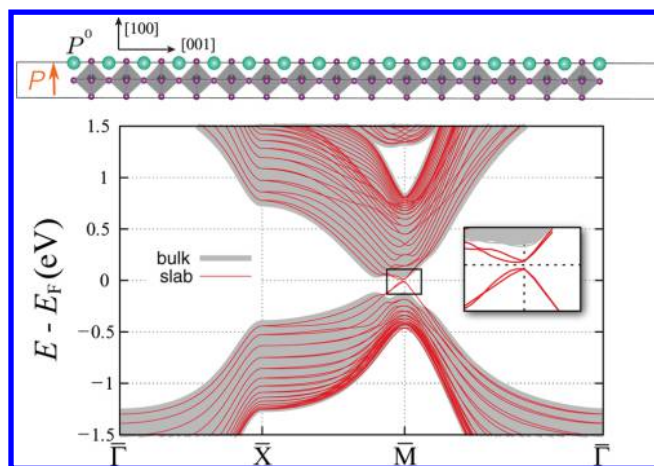


**Figure 2.** Electronic structure of nonpolar surfaces of CsPbI<sub>3</sub>. The surface normal is along the [001] direction. The shaded (gray) bands correspond to bulk bands. The red lines highlight the slab bands. The topological surface states emerge inside the bulk band gap. The tiny gap of the surface states (magnified in inset) appears due to the finite slab thickness.

energy the Dirac cone (p-type) associated with the  $P^-$  surface and downward in energy the Dirac cone (n-type) associated with the  $P^+$  surface. This feature resembles the electronic structures found in graphene/ferroelectric/graphene composite<sup>28</sup> and gives rise to nontrivial spin textures for bands near the Fermi energy. For instance, the surface states of the  $P^-$  and  $P^+$  surfaces are expected to have the same spin helicity at the Fermi energy, as shown schematically in the inset of Figure 3b. This is confirmed by our first-principles calculations (Figure 3c). Similar to nonferroelectric topological insulators, currents on the  $P^-$  and  $P^+$  surfaces carry opposite spins (Figure 3d). Ferroelectricity allows these currents to be separated in energy as well. These results demonstrate that strained CsPbI<sub>3</sub> is a FETI with TSSs strongly coupled to bulk polarization.

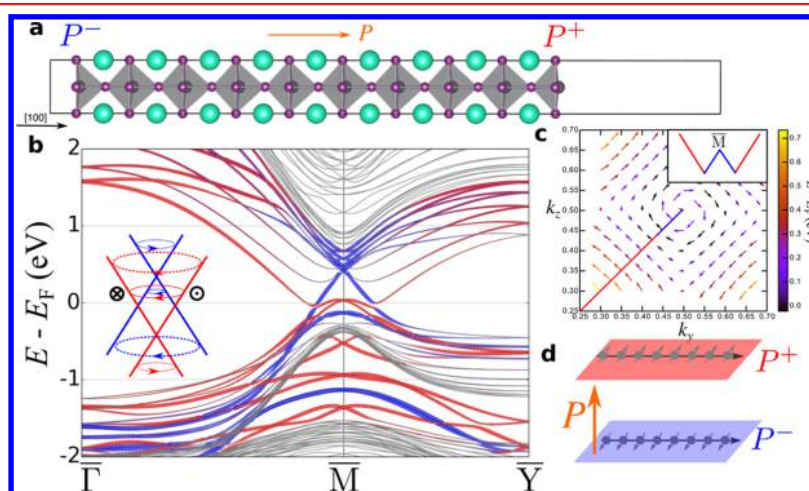


**Figure 3.** Electronic structure of polar surfaces in CsPbI<sub>3</sub>. (a) Schematic of the slab geometry with surface normal and polarization along the [100] direction, creating  $P^-$  surface (left) and  $P^+$  surface (right). (b) Surface band structure. The red and blue lines represent the contributions of surface states from the  $P^+$  surface and  $P^-$  surface, respectively. The thickness of lines scales with the contribution. The inset illustrates the vertically shifted Dirac cones on the  $P^+$  and  $P^-$  surfaces. The energies of TSSs depend on the excess surface charges on the polar surfaces. Because the TSS is robust to nonmagnetic perturbations, the presence of the TSS is guaranteed regardless of the surface termination of CsPbI<sub>3</sub>. (c) DFT spin texture for the lowest conduction band around M. The solid line denotes the  $\Gamma$ -M direction. (d) Orientations of spin currents on polar surfaces. The spins on  $P^+$  and  $P^-$  surfaces adopt opposite orientations for spin currents along the same direction.

We further explore the possible realization of a FETI by applying hydrostatic pressure to CsPbI<sub>3</sub>. The pressure-driven phase transition is studied by calculating the pressure-dependent formation enthalpy ( $H$ ) for crystals with the following symmetries: the cubic paraelectric  $Pm\bar{3}m$  phase, three tetragonal phases,  $P4mm$  (that supports ferroelectric distortion along [001]),  $I4/mcm$  (that supports antiferrodistortive rotation of the iodine octahedra), and  $I4cm$  (that supports both polar displacement and antiferrodistortive iodine octahedra), rhombohedral  $R3mR$  phase (that supports ferroelectric distortion along [111]), two orthorhombic phases,  $Pbnm$  (perovskite structure with tilted corner-sharing iodine octahedra,  $a^-a^-c^+$  in Glazer's naming scheme), and the  $Pnma$  phase (nonperovskite structure with edge-sharing iodine octahedra, room-temperature phase of CsPbI<sub>3</sub>). Figure 4 presents the relative formation enthalpy ( $\Delta H = H - H_{Pm\bar{3}m}$ ), and the band gap for each phase as a function of pressure. We find that  $Pnma$  phase is always the most stable phase across the pressure range studied (0–10 GPa), and has a large band gap throughout. This implies that applying homogeneous hydrostatic pressure alone would not induce a topological phase transition in CsPbI<sub>3</sub>. In comparison,  $Pm\bar{3}m$ ,  $P4mm$ ,  $R3mR$ ,  $I4cm$ , and  $I4/mcm$  phases all exhibit pressure-induced band gap closure, a signature of topological phase transition. Further, Berry's phase calculations show that only the  $P4mm$  phase has significant polarization (0.06 C/m<sup>2</sup>) at high pressure (9 GPa). These findings suggest that the key to achieving FETI in CsPbI<sub>3</sub> is to suppress the PbI<sub>6</sub> cage rotation in perovskite structure. Nanoscale materials growth of the lead halides is commonly performed.<sup>29,30</sup> Recent experimental studies show that it is possible to stabilize the edge-sharing perovskite phase of CsPbI<sub>3</sub> under room temperature in nanocrystal form<sup>24</sup> or single crystals in an inert atmosphere.<sup>25</sup> Additionally, strain tuning of ferroelectric thin films is routinely carried out.<sup>31</sup> In particular, nanoindentation experiments have shown that CsPbI<sub>3</sub> single crystals are stable under pressure.<sup>32</sup> These provide an opportunity to obtain FETI through appropriate strain engineering.

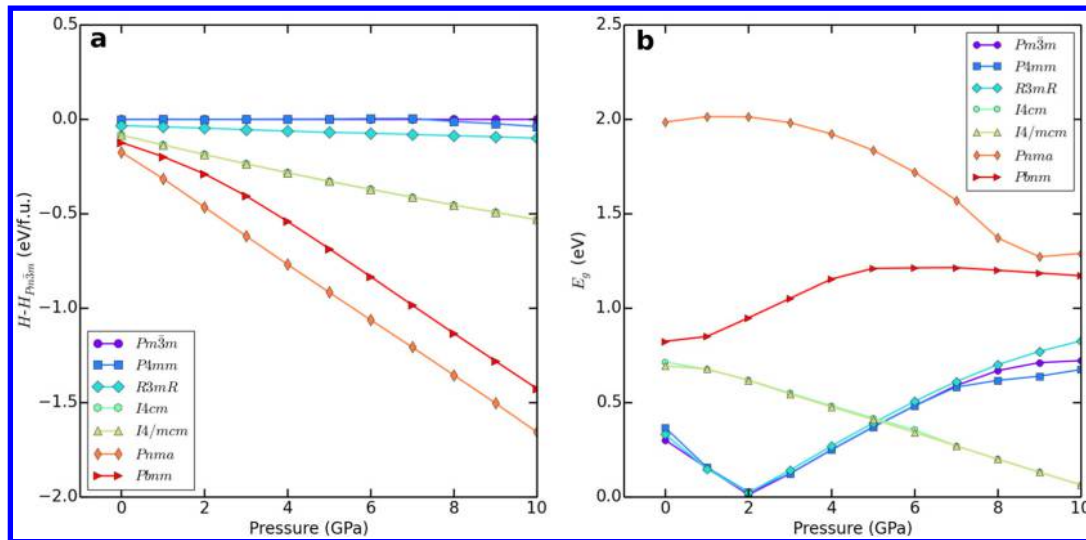


**Figure 4.** Pressure driven phase transition of CsPbI<sub>3</sub>. (a) Relative formation enthalpy  $\Delta H$  as referenced to cubic paraelectric  $Pm\bar{3}m$  phase. (b) Evolution of the band gap as a function of pressure.

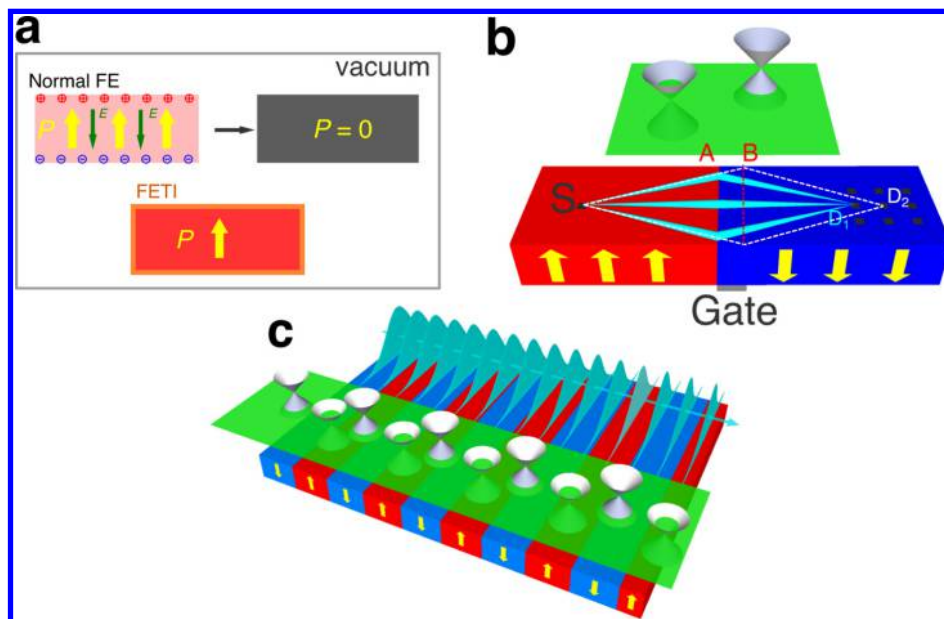


**Figure 5.** Schematic of functional devices based on ferroelectric topological insulator. (a) Robust ferroelectricity of FETI under open circuit condition. Ferroelectric thin film normal insulator (FENI) becomes paraelectric in vacuum due to the large depolarization field. The polarization of FETI is protected with metallic surface states serving as intrinsic metallic leads. (b) Domain wall in FETI as Veselago lens. Electrons injected at S will focus at D<sub>1</sub> for domain wall positioned at line A. The domain wall can be moved to line B by reversing the direction of the polarization through a gate voltage. The focusing point will consequently be shifted to D<sub>2</sub>. (c) Ferroelectric domain arrays as nanoscale topological p–n junction arrays for electron beam supercollimation. The potential periodicity and amplitude can be tuned by varying the size of domain and the magnitude of the polarization, respectively.

We now comment on the possible applications of FETI. Compared to a ferroelectric normal insulator (FENI), the FETI is expected to have more robust ferroelectricity. As shown in Figure 5a, normal ferroelectric thin films (e.g., PbTiO<sub>3</sub>) are unstable under ideal open-circuit conditions (in vacuum) due to the large depolarization field.<sup>33,34</sup> In practice, normal ferroelectrics are stabilized by electrodes or surface charges that eliminate the effect of the bound charges. An advantage of the FETI over the FENI is the guaranteed presence of metallic surface states, which can serve as innate metallic electrodes to create an intrinsic short-circuit condition, allowing for

automatic surface charge dissipation and hence stable ferroelectricity in vacuum.

The polarity of ferroelectric surfaces can be tuned and reversed by well-controlled external stimuli, such as electric field, stress field, and temperature. Therefore, the coupling of switchable polarization and TSSs in FETI offers a powerful paradigm for novel device engineering. For example, the 180° domain wall in FETI may serve as a Veselago lens<sup>35</sup> for precise focusing of electric current. Shown in Figure 5b, the 180° domain wall separates domains with opposite polarities, thus creating an n-type Dirac cone on the P<sup>+</sup> surface and a p-type Dirac cone on the P<sup>-</sup> surface. Perfect focusing of electric

current occurs when the n-type and p-type Fermi circles have the same radius.<sup>36</sup> While this condition can only be obtained by careful tuning of local chemical potentials in graphene, it is automatically satisfied in FETIs because of the antisymmetric nature of the  $P^+$  and  $P^-$  surfaces. By moving the position of the domain wall via a gate voltage, it is possible to controllably change the focusing point on the  $P^-$  surface.

In addition, ferroelectric materials can be patterned into designed multidomain configurations. This enables simplified fabrication and control of high-density p–n junction arrays at the nanoscale (Figure 5c), which may find applications in electronics and spintronics, such as electron beam supercollimation.<sup>37,38</sup> The operating bandwidth of Dirac Fermion-based electron beam supercollimators increases as the period of the p–n arrays decreases.<sup>37</sup> This has proved to be a limiting constraint in designing graphene-based electron beam supercollimators using conventional metallic gates that are usually larger than 100 nm in size. By contrast, nanoscale ferroelectric domains can be easily created and manipulated,<sup>23,39</sup> opening possibilities for spin-sensitive electronic devices of wide operating bandwidth.

In conclusion, our ab initio calculations demonstrate that it is possible to realize ferroelectricity and robust topological surface states in a single material. The electronic structure of cubic CsPbI<sub>3</sub> with ferroelectric distortions at high pressure can act as a prototype for designing ferroelectric topological insulators that are stable at ambient conditions. Replacing Cs with larger cations (e.g., molecular cation, (CH<sub>3</sub>)<sub>4</sub>N<sup>+</sup>) may help to suppress PbI<sub>6</sub> octahedron rotation. The discovery of a robust material realization of ferroelectric topological insulators can potentially lead to new device applications in electronics and spintronics.

**Methods.** DFT calculations are carried out with plane-wave density functional theory packages QUANTUM-ESPRESSO<sup>40</sup> and ABINIT<sup>41</sup> with Perdew–Burke–Ernzerhof (PBE)<sup>42</sup> density functional and norm conserving, optimized,<sup>43</sup> designed nonlocal<sup>44</sup> pseudopotentials generated from the OPIUM package. A plane-wave energy cutoff of 50 Ry is used. A five-atom unit cell is used for constructing the structural and topological phase diagram of cubic CsPbI<sub>3</sub> with the PbI<sub>6</sub> octahedron rotation suppressed. An  $8 \times 8 \times 8$  Monkhorst–Pack  $k$ -point grid is used to converge the charge density, while an  $8 \times 8 \times 8$  Monkhorst–Pack wavevector coarse grid, interpolated to a  $32 \times 32 \times 32$  fine grid, is used for calculations of the phonon entropy. A supercell slab method is used to calculate the band structures of surface states. Atoms in the slab model are fixed to their bulk positions. The supercell for modeling the nonpolar surface consists of 30 layers of ferroelectric CsPbI<sub>3</sub> and 22 Å of vacuum. The slab has surface normal along the [001] direction and the polarization along the [100] direction. The polar surfaces are modeled with a slab that has both surface normal and polarization oriented along the [100] direction. The vacuum inside the supercell is 15 Å thick, and the dipole correction<sup>45</sup> is applied to remove the spurious interaction between different images. The surface band structure of polar surfaces is projected onto orthogonalized atomic wave functions, and the weight of atomic wave functions from  $P^+$  and  $P^-$  surface atoms are then evaluated separately for 30 highest valence bands and 10 lowest conduction bands.

## ■ ASSOCIATED CONTENT

### Supporting Information

The Supporting Information is available free of charge on the ACS Publications website at DOI: 10.1021/acs.nanolett.5b04545.

Atomic coordinates of all crystal structures at 0 GPa. (PDF)

## ■ AUTHOR INFORMATION

### Corresponding Authors

\*E-mail: sliu@carnegiescience.edu.

\*E-mail: rappe@sas.upenn.edu.

### Notes

The authors declare no competing financial interest.

## ■ ACKNOWLEDGMENTS

S.L. was supported by the NSF through Grant CBET-1159736 and Carnegie Institution for Science. Y.K. was supported by the NSF through Grant DMR-1120901. L.Z.T. was supported by the U.S. DOE under Grant DE-FG02-07ER46431. A.M.R. was supported by the U.S. ONR under Grant N00014-14-1-0761. Computational support was provided by the U.S. DOD through a Challenge Grant from the HPCMO and by the U.S. DOE through computer time at NERSC.

## ■ REFERENCES

- (1) Hasan, M. Z.; Kane, C. L. *Rev. Mod. Phys.* **2010**, *82*, 3045–3067.
- (2) Zhu, Z.; Cheng, Y.; Schwingschögl, U. *Phys. Rev. B: Condens. Matter Mater. Phys.* **2012**, *85*, 235401–5.
- (3) Fu, L.; Kane, C. L.; Mele, E. J. *Phys. Rev. Lett.* **2007**, *98*, 106803–4.
- (4) Hsieh, D.; Qian, D.; Wray, L.; Xia, Y.; Hor, Y. S.; Cava, R. J.; Hasan, M. Z. *Nature* **2008**, *452*, 970–974.
- (5) Zhang, H. J.; Liu, C. X.; Qi, X. L.; Dai, X.; Fang, Z.; Zhang, S. C. *Nat. Phys.* **2009**, *5*, 438–442.
- (6) Chen, Y. L.; Analytis, J. G.; Chu, J. H.; Liu, Z. K.; Mo, S. K.; Qi, X. L.; Zhang, H. J.; Lu, D. H.; Dai, X.; Fang, Z.; Zhang, S. C.; Fisher, I. R.; Hussain, Z.; Shen, Z. X. *Science* **2009**, *325*, 178–181.
- (7) Xia, Y.; Qian, D.; Hsieh, D.; Wray, L.; Pal, A.; Lin, H.; Bansil, A.; Grauer, D.; Hor, Y. S.; Cava, R. J.; Hasan, M. Z. *Nat. Phys.* **2009**, *5*, 398–402.
- (8) Yan, B.; Jansen, M.; Felser, C. *Nat. Phys.* **2013**, *9*, 709–711.
- (9) Shitade, A.; Katsura, H.; Kuneš, J.; Qi, X.-L.; Zhang, S.-C.; Nagaosa, N. *Phys. Rev. Lett.* **2009**, *102*, 256403–4.
- (10) Carter, J.-M.; Shankar, V. V.; Zeb, M. A.; Kee, H.-Y. *Phys. Rev. B: Condens. Matter Mater. Phys.* **2012**, *85*, 115105–6.
- (11) Yang, B.-J.; Kim, Y. B. *Phys. Rev. B: Condens. Matter Mater. Phys.* **2010**, *82*, 085111–11.
- (12) Chadov, S.; Qi, X.; Kübler, J.; Fecher, G. H.; Felser, C.; Zhang, S. C. *Nat. Mater.* **2010**, *9*, 541–545.
- (13) Yang, K.; Setyawan, W.; Wang, S.; Nardelli, M. B.; Curtarolo, S. *Nat. Mater.* **2012**, *11*, 614–619.
- (14) Jin, H.; Im, J.; Freeman, A. J. *Phys. Rev. B: Condens. Matter Mater. Phys.* **2012**, *86*, 121102–5.
- (15) Bahramy, M.; Yang, B.-J.; Arita, R.; Nagaosa, N. *Nat. Commun.* **2012**, *3*, 679.
- (16) Piskunov, S.; Heifets, E.; Eglitis, R.; Borstel, G. *Comput. Mater. Sci.* **2004**, *29*, 165–178.
- (17) Bennett, J. W.; Grinberg, I.; Rappe, A. M. *J. Am. Chem. Soc.* **2008**, *130*, 17409–17412.
- (18) Wang, F.; Grinberg, I.; Rappe, A. M. *Appl. Phys. Lett.* **2014**, *104*, 152903.
- (19) Grinberg, I.; West, D. V.; Torres, M.; Gou, G.; Stein, D. M.; Wu, L.; Chen, G.; Gallo, E. M.; Akbashev, A. R.; Davies, P. K.; Spanier, J. E.; Rappe, A. M. *Nature* **2013**, *503*, 509–512.

- (20) Bennett, J. W.; Garrity, K. F.; Rabe, K. M.; Vanderbilt, D. *Phys. Rev. Lett.* **2012**, *109*, 167602.
- (21) Xu, B.; Singh, D. J.; Cooper, V. R.; Feng, Y. P. *Europhys. Lett.* **2011**, *94*, 37006.
- (22) Wang, J.; Chen, X.; Zhu, B.-F.; Zhang, S.-C. *Phys. Rev. B: Condens. Matter Mater. Phys.* **2012**, *85*, 235131.
- (23) Xu, R.; Liu, S.; Grinberg, I.; Karthik, J.; Damodaran, A. R.; Rappe, A. M.; Martin, L. W. *Nat. Mater.* **2014**, *14*, 79–86.
- (24) Protesescu, L.; Yakunin, S.; Bodnarchuk, M. I.; Krieg, F.; Caputo, R.; Hendon, C. H.; Yang, R. X.; Walsh, A.; Kovalenko, M. V. *Nano Lett.* **2015**, *15*, 3692–3696.
- (25) Eperon, G. E.; Paternò, G. M.; Sutton, R. J.; Zampetti, A.; Haghighirad, A. A.; Cacialli, F.; Snaith, H. J. *J. Mater. Chem. A* **2015**, *3*, 19688–19695.
- (26) Murakami, S. *New J. Phys.* **2007**, *9*, 356.
- (27) Soluyanov, A. A.; Vanderbilt, D. *Phys. Rev. B: Condens. Matter Mater. Phys.* **2011**, *83*, 235401.
- (28) Baeumer, C.; Saldana-Greco, D.; Martinez, J. M. P.; Rappe, A. M.; Shim, M.; Martin, L. W. *Nat. Commun.* **2015**, *6*, 6136.
- (29) Akkerman, Q. A.; D’Innocenzo, V.; Accornero, S.; Scarpellini, A.; Petrozza, A.; Prato, M.; Manna, L. *J. Am. Chem. Soc.* **2015**, *137*, 10276–10281.
- (30) Nedelcu, G.; Protesescu, L.; Yakunin, S.; Bodnarchuk, M. I.; Grotevent, M. J.; Kovalenko, M. V. *Nano Lett.* **2015**, *15*, 5635–5640.
- (31) Schlom, D. G.; Chen, L. Q.; Eom, C. B.; Rabe, K. M.; Streiffer, S. K.; Triscone, J. M. *Annu. Rev. Mater. Res.* **2007**, *37*, 589–626.
- (32) Rakita, Y.; Cohen, S. R.; Kedem, N. K.; Hodes, G.; Cahen, D. *MRS Commun.* **2015**, *5*, 623–629.
- (33) Kolpak, A. M.; Sai, N.; Rappe, A. M. *Phys. Rev. B: Condens. Matter Mater. Phys.* **2006**, *74*, 054112.
- (34) Levchenko, S. V.; Rappe, A. M. *Phys. Rev. Lett.* **2008**, *100*, 256101.
- (35) Veselago, V. G. *Soviet Physics Uspekhi* **1968**, *10*, 509–514.
- (36) Cheianov, V. V.; Fal’ko, V.; Altshuler, B. *Science* **2007**, *315*, 1252–1255.
- (37) Park, C.-H.; Son, Y.-W.; Yang, L.; Cohen, M. L.; Louie, S. G. *Nano Lett.* **2008**, *8*, 2920–2924.
- (38) Park, C.-H.; Yang, L.; Son, Y.-W.; Cohen, M. L.; Louie, S. G. *Nat. Phys.* **2008**, *4*, 213–217.
- (39) Catalan, G.; Seidel, J.; Ramesh, R.; Scott, J. F. *Rev. Mod. Phys.* **2012**, *84*, 119–156.
- (40) Giannozzi, P.; et al. *J. Phys.: Condens. Matter* **2009**, *21*, 395502.
- (41) Gonze, X.; et al. *Comput. Phys. Commun.* **2009**, *180*, 2582–2615.
- (42) Perdew, J. P.; Burke, K.; Ernzerhof, M. *Phys. Rev. Lett.* **1996**, *77*, 3865–3868.
- (43) Rappe, A. M.; Rabe, K. M.; Kaxiras, E.; Joannopoulos, J. D. *Phys. Rev. B: Condens. Matter Mater. Phys.* **1990**, *41*, 1227–1230.
- (44) Ramer, N. J.; Rappe, A. M. *Phys. Rev. B: Condens. Matter Mater. Phys.* **1999**, *59*, 12471–12478.
- (45) Bengtsson, L. *Phys. Rev. B: Condens. Matter Mater. Phys.* **1999**, *59*, 12301–12304.